SINTEF
PROCEEDINGS
2

Proceedings of the 12th International Conference on Computational Fluid Dynamics in the Oil & Gas, Metallurgical and Process Industries

Progress in Applied CFD – CFD2017

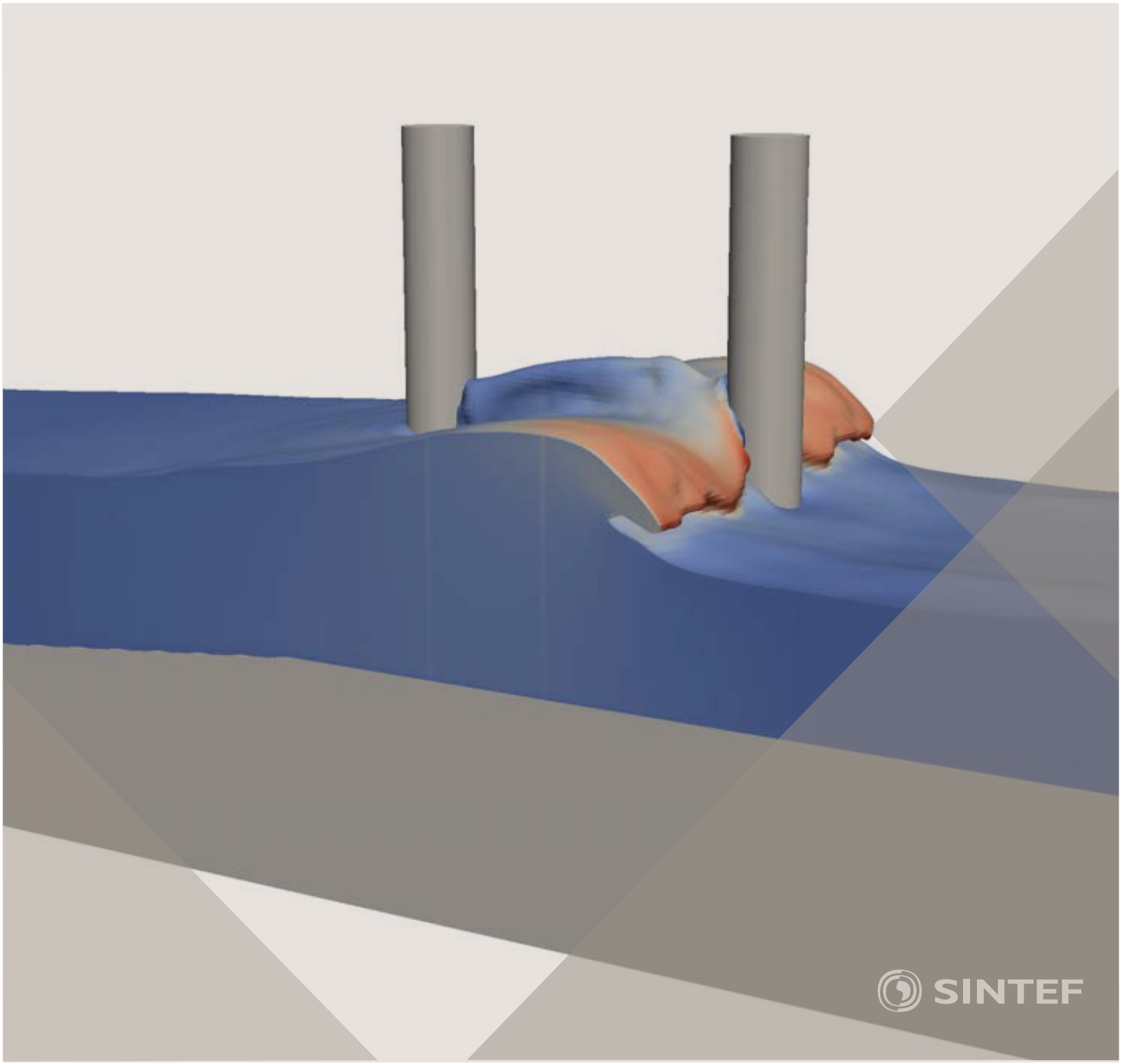

SINTEF Proceedings

Editors:
Jan Erik Olsen and Stein Tore Johansen

Progress in Applied CFD – CFD2017

Proceedings of the 12th International Conference on Computational Fluid Dynamics in the Oil & Gas, Metallurgical and Process Industries

SINTEF Academic Press

SINTEF Proceedings no 2
Editors: Jan Erik Olsen and Stein Tore Johansen
Progress in Applied CFD – CFD2017
Selected papers from 10th International Conference on Computational Fluid Dynamics in the Oil & Gas, Metallurgical and Process Industries

Key words:
CFD, Flow, Modelling

Cover, illustration: Arun Kamath

ISSN 2387-4295 (online)
ISBN 978-82-536-1544-8 (pdf)

SINTEF Academic Press
Address: Forskningsveien 3 B
PO Box 124 Blindern
N-0314 OSLO
Tel: +47 73 59 30 00
Fax: +47 22 96 55 08

www.sintef.no/byggforsk
www.sintefbok.no

SINTEF Proceedings
SINTEF Proceedings is a serial publication for peer-reviewed conference proceedings on a variety of scientific topics.
The processes of peer-reviewing of papers published in SINTEF Proceedings are administered by the conference organizers and proceedings editors. Detailed procedures will vary according to custom and practice in each scientific community.

PREFACE

This book contains all manuscripts approved by the reviewers and the organizing committee of the 12th International Conference on Computational Fluid Dynamics in the Oil & Gas, Metallurgical and Process Industries. The conference was hosted by SINTEF in Trondheim in May/June 2017 and is also known as CFD2017 for short. The conference series was initiated by CSIRO and Phil Schwarz in 1997. So far the conference has been alternating between CSIRO in Melbourne and SINTEF in Trondheim. The conferences focuses on the application of CFD in the oil and gas industries, metal production, mineral processing, power generation, chemicals and other process industries. In addition pragmatic modelling concepts and bio-mechanical applications have become an important part of the conference. The papers in this book demonstrate the current progress in applied CFD.

The conference papers undergo a review process involving two experts. Only papers accepted by the reviewers are included in the proceedings. 108 contributions were presented at the conference together with six keynote presentations. A majority of these contributions are presented by their manuscript in this collection (a few were granted to present without an accompanying manuscript).

The organizing committee would like to thank everyone who has helped with review of manuscripts, all those who helped to promote the conference and all authors who have submitted scientific contributions. We are also grateful for the support from the conference sponsors: ANSYS, SFI Metal Production and NanoSim.

Stein Tore Johansen & Jan Erik Olsen

Organizing committee:

Conference chairman: Prof. Stein Tore Johansen
Conference coordinator: Dr. Jan Erik Olsen
Dr. Bernhard Müller
Dr.Sigrid Karstad Dahl
Dr.Shahriar Amini
Dr.Ernst Meese
Dr.Josip Zoric
Dr.Jannike Solsvik
Dr.Peter Witt

Scientific committee:

Stein Tore Johansen, SINTEF/NTNU
Bernhard Müller, NTNU
Phil Schwarz, CSIRO
Akio Tomiyama, Kobe University
Hans Kuipers, Eindhoven University of Technology
Jinghai Li, Chinese Academy of Science
Markus Braun, Ansys
Simon Lo, CD-adapco
Patrick Segers, Universiteit Gent
Jiyuan Tu, RMIT
Jos Derksen, University of Aberdeen
Dmitry Eskin, Schlumberger-Doll Research
Pär Jönsson, KTH
Stefan Pirker, Johannes Kepler University
Josip Zoric, SINTEF

CONTENTS

IMMERSED BOUNDARY METHOD FOR THE COMPRESSIBLE NAVIER–STOKES EQUATIONS USING HIGH ORDER SUMMATION-BY-PARTS DIFFERENCE OPERATORS

M. EHSAN KHALILI[1*], **MARTIN LARSSON**[2†], **BERNHARD MÜLLER**[1‡]

[1]Department of Energy and Process Engineering, Norwegian University of Science and Technology (NTNU), Kolbjørn Hejes vei 2, NO-7491 Trondheim, Norway

[2]Sportradar AS, Ferjemannsveien 10, NO-7014 Trondheim, Norway

* E-mail: mohammadtaghi.khalili@ntnu.no
† E-mail: m.larsson@sportradar.com
‡ E-mail: bernhard.muller@ntnu.no

ABSTRACT

A ghost-point immersed boundary method is devised for the compressible Navier–Stokes equations by employing high order summation-by-parts (SBP) difference operators. The immersed boundaries are treated as sharp interfaces by enforcing the solid wall boundary conditions via flow variables at ghost points using bilinearly interpolated flow variables at mirror points. The approach is verified and validated for compressible flow past a circular cylinder at moderate Reynolds numbers.

Keywords: High order finite difference method, Immersed boundary method, Compressible viscous flow .

NOMENCLATURE

Greek Symbols

ρ	Mass density
μ	Dynamic viscosity
τ	Viscous stress tensor
γ	Ratio of specific heats
κ	Heat conduction coefficient
ϕ	Generic variable
$\mathcal{G}$	Set of body intercept points that are part of the interpolation stencil
Λ	Parameter
σ	Source term in steady state heat equation
ξ, η	Transformed coordinates in computational domain

Latin Symbols

t	Physical time
E	Specific total energy
H	Total entalpy
p	Pressure
S_c	Sutherland constant
T	Temperature
$\mathbf{U}$	Vector of conservative variables
$\mathbf{V}$	Vandermonde matrix
x, y	Cartesian coordinates in physical domain
J^{-1}	Jacobian determinant

Sub/superscripts

GP	Ghost point
IP	Image point
BI	Body intercept
c'	Conservative perturbation
ν'	Viscous perturbation

INTRODUCTION

Many applications in engineering, biology and medicine involve low and moderate Reynolds number flow problems with complex boundaries between fluid and structure. Simulating these problems with conventional methods requires the process of generating high quality and body-conforming grids which is challenging and time-consuming. Recently, there has been a growing interest in the development of non-boundary conforming methodologies for the solution of the Navier–Stokes equations (Mittal and Iaccarino, 2005). In such methods, the requirement that the grid should conform to a solid boundary is dropped, and the effect of the immersed boundary of the solid body on the flow is introduced through the proper treatment of the solution variables near the boundary. The basic advantage of these formulations is the simplicity compared with conventional body-conforming grid generation, especially in cases of complex stationary or moving boundaries where the demand for regeneration or deformation of the grid is eliminated. Therefore, efficient non boundary conforming strategies with robust Cartesian coordinate solvers can directly be applied to a wide range of flow problems.

Over the past decades a variety of non-body conforming approaches with various degrees of accuracy and complexity have been proposed. The so-called immersed-boundary method (IBM) was introduced by (Peskin, 1972). IB methods are categorized into continuous forcing and discrete (direct) forcing approaches. In the first category, a continuous forcing term is added to the governing equations to represent the interaction between the immersed boundary and the fluid, and a discrete Dirac–delta function is used to smooth this singular force on the Euler grid (Peskin, 1972; Goldstein *et al.*, 1993; Saiki and Biringen, 1996). Numerous modifications and improvements have been implemented in this category (Haeri and Shrimpton, 2012; Sotiropoulos and Yang, 2014). The second category, including the sharp interface method, mimics the presence of a surface force exerted by the boundary on the fluid by adjusting the discretization in the vicinity of the immersed boundary in order to directly take into account the boundary conditions at the IB (Ye *et al.*, 1999; Fadlun *et al.*, 2000; Mohd-Yusof, 1997; Balaras, 2004). The ghost cell immersed boundary (GCIB) method as sharp interface method is proposed in the studies by (Tseng and Ferziger, 2003; Ghias *et al.*, 2007; Mittal *et al.*, 2008). Ghost cells are defined as a layer of cells within the solid body having at least one nearby point in the fluid domain

i.e., adjoining to the immersed boundary. The flow variables at the ghost points are calculated with the boundary conditions at the immersed boundary and the flow variables at grid points near the IB in the fluid domain. The presence of the immersed boundary is introduced by the flow variables at the ghost points. The idea of image points inside the fluid domain is adopted to ensure suitable weighting coefficients in the reconstruction formula in order to avoid numerical instability caused by the large, negative weighting coefficients in the extrapolation formulation (Tseng and Ferziger, 2003). The ghost point method has shown large potential to deal with different fluid-solid interaction problems, including those involving highly complex geometries and moving or deforming bodies (Mittal *et al.*, 2008).

In the IBM, all the equations can be solved on a body nonconformal, Cartesian grid which does not require to be updated for moving or deforming bodies. Due to the flexibility of the method, many different types of IBM have been developed in incompressible and compressible flow solvers. However, most of the attention on IBM is devoted to incompressible flows (Mittal and Iaccarino, 2005). Works on viscous compressible flows are still scarce and a few IBM for viscous compressible flows has been developed (De Palma *et al.*, 2006; Ghias *et al.*, 2007; de Tullio *et al.*, 2007; Brehm *et al.*, 2015). Due to the different nature of the Navier–Stokes equations for compressible and incompressible flows, i.e. the requirement of equation of state for compressible flows, there are differences in implementation of the boundary conditions between these two types of equations as well as in the spatial discretisation schemes employed.

In this study, the ghost point IB approach has been adopted for a high order finite difference method based on summation-by-parts operators (SBP) to provide an accurate and efficient approach for studying low Mach number compressible viscous flows. The major ambition of the present work is to extend this approach for fluid structure interaction (FSI) in the upper airways to study the obstructive sleep apnea syndrome. The main focus in our study is subsonic flow which permits us to characterize the acoustic wave propagation induced by the structure oscillation in FSI to obtain a better understanding of snoring. The proposed approach is verified and validated for two dimensional flows over a circular cylinder. In the following sections, a brief review of the governing equations and their numerical solution is given. Then, the IB approach is described in detail. Finally, results are provided and compared with numerical and experimental ones available in the literature.

MODEL DESCRIPTION

Governing equations

The 2D compressible Navier–Stokes equations in perturbation form are solved. To minimize cancellation errors when discretizing the Navier–Stokes equations for compressible low Mach number flow, the perturbation formulation is employed (Sesterhenn *et al.*, 1999; Müller, 2008). The conservative form of the 2D compressible Navier–Stokes equations in perturbation formulation can be written as

$$\mathbf{U}'_t + \mathbf{F}^{c\prime}_x + \mathbf{G}^{c\prime}_y = \mathbf{F}^{v\prime}_x + \mathbf{G}^{v\prime}_y \tag{1}$$

where $\mathbf{U}' = \mathbf{U} - \mathbf{U_0}$ is the vector of conservative perturbation variables with $\mathbf{U} = (\rho, \rho u, \rho v, \rho E)^T$ the vector of the conservative variables and $\mathbf{U}_0 = (\rho_0, 0, 0, (\rho E)_0)^T$ the stagnation values.

The conservative perturbation variables $\mathbf{U}'$ and the inviscid ($\mathbf{F}^{c\prime}$, $\mathbf{G}^{c\prime}$) and viscous perturbation flux vectors ($\mathbf{F}^{v\prime}$, $\mathbf{G}^{v\prime}$) are defined by $\mathbf{F}^{c\prime} = \mathbf{F}^c(\mathbf{U}) - \mathbf{F}^c(\mathbf{U_0})$, etc.

$$\mathbf{U}' = \begin{pmatrix} \rho' \\ (\rho u)' \\ (\rho v)' \\ (\rho E)' \end{pmatrix},$$

$$\mathbf{F}^{c\prime} = \begin{pmatrix} (\rho u)' \\ (\rho u)'u' + p' \\ (\rho v)'u' \\ ((\rho H)_0 + (\rho H)')u' \end{pmatrix}, \mathbf{G}^{c\prime} = \begin{pmatrix} (\rho v)' \\ (\rho u)'v' \\ (\rho v)'v' + p' \\ ((\rho H)_0 + (\rho H)')v' \end{pmatrix},$$

$$\mathbf{F}^{v\prime} = \begin{pmatrix} 0 \\ \tau'_{xx} \\ \tau'_{xy} \\ u'\tau'_{xx} + v'\tau'_{xy} + \kappa T'_x \end{pmatrix}, \mathbf{G}^{v\prime} = \begin{pmatrix} 0 \\ \tau'_{yx} \\ \tau'_{yy} \\ u'\tau'_{yx} + v'\tau'_{yy} + \kappa T'_y \end{pmatrix},$$

where t is physical time and x and y are the Cartesian coordinates. ρ denotes density, u and v the x- and y-direction velocity components, E the specific total energy, T the temperature and κ the heat conduction coefficient calculated from the constant Prandtl number $\mathrm{Pr} = 0.72$. ρ_0, $(\rho E)_0$ and $(\rho H)_0$ denote the stagnation values of density, total energy density and total enthalpy density. The perturbation variables are defined as:

$$\rho' = \rho - \rho_0, \quad (\rho\mathbf{u})' = (\rho\mathbf{u}),$$

$$(\rho E)' = \rho E - (\rho E)_0, \quad (\rho H)' = (\rho E)' + p', \quad \mathbf{u}' = \frac{(\rho\mathbf{u})'}{\rho_0 + \rho'},$$

$$\tau' = \mu(\nabla\mathbf{u}' + (\nabla\mathbf{u}')^T) - \frac{2}{3}\mu(\nabla\cdot\mathbf{u}')\mathbf{I}, \quad T' = \frac{p'/R - \rho' T_0}{\rho_0 + \rho'}$$

Here, R is the specific gas constant and μ is the viscosity which is determined from the Sutherland law $\frac{\mu}{\mu_0} = (\frac{T}{T_0})^{1.5}[(1+S_c)/(\frac{T}{T_0}+S_c)]$ with the non-dimensional Sutherland constant $S_c = \frac{110}{301.75}$.

Since perfect gas is considered, the pressure perturbation can be related to the conservative perturbation variables by $p' = (\gamma-1)[(\rho E)' - \frac{1}{2}((\rho\mathbf{u}'\cdot\mathbf{u}'))]$, where the ratio of specific heats $\gamma = c_p/c_v = 1.4$ for air.

The viscous flux vectors $\mathbf{F}^{v\prime}$ and $\mathbf{G}^{v\prime}$ are the same as for the standard conservative form, except for using the temperature perturbation T' instead of temperature T for the heat flux terms. The momentum density and velocity perturbations are taken as the same as their unperturbed counterparts, i.e. $(\rho\mathbf{u})' = \rho\mathbf{u}$ (Larsson and Müller, 2009). For convenience the variables are non-dimensionalized with ρ_0, stagnation speed of sound c_0 and $\rho_0 c_0^2$ as reference values. In order to generalize the geometry for non-uniform Cartesian grids, the equations of motions are transformed from the physical domain (x,y) to the computational domain (ξ,η) by the following relations,

$$\begin{aligned} x &= x(\xi,\eta) \\ y &= y(\xi,\eta) \end{aligned} \tag{2}$$

Thus, the transformed 2D compressible Navier–Stokes equations in perturbation form are expressed as:

$$\hat{\mathbf{U}}'_t + \hat{\mathbf{F}}'_\xi + \hat{\mathbf{F}}'_\eta = 0 \tag{3}$$

where $\hat{\mathbf{U}}' = J^{-1}\mathbf{U}'$, $\hat{\mathbf{F}}' = J^{-1}(\xi_x(\mathbf{F}^{c\prime} - \mathbf{F}^{v\prime}) + \xi_y(\mathbf{G}^{c\prime} - \mathbf{G}^{v\prime}))$ and $\hat{\mathbf{G}}' = J^{-1}(\eta_x(\mathbf{F}^{c\prime} - \mathbf{F}^{v\prime}) + \eta_y(\mathbf{G}^{c\prime} - \mathbf{G}^{v\prime}))$. The chain rule for partial differentiation provides the expressions for Cartesian derivatives in the viscous flux vectors $\mathbf{F}^{v\prime}$ and $\mathbf{G}^{v\prime}$, e.g.

$u'_x = u'_\xi \xi_x + u'_\eta \eta_x$ and $u'_y = u'_\xi \xi_y + u'_\eta \eta_y$. The Jacobian determinant of the transformation is $J^{-1} = x_\xi y_\eta - x_\eta y_\xi$ and metric terms are

$$\begin{aligned} J^{-1}\xi_x &= y_\eta, \quad J^{-1}\xi_y = -x_\eta, \\ J^{-1}\eta_x &= -y_\xi, \quad J^{-1}\eta_y = x_\xi. \end{aligned} \tag{4}$$

Numerical methodology

The summation-by-parts (SBP) operator Q is an approximation to the first ξ- and η- derivatives in (4) and (3). In the interior, it corresponds to the standard sixth order central operator, while being third order accurate near the boundaries. Through a special boundary treatment, SBP operators permit energy estimates for discrete problems similar to those for the continuous ones that are approximated. Therefore, SBP operators can yield strictly stable schemes for general boundary conditions (Strand, 1994; Gustafsson *et al.*, 1995; Gustafsson, 2008). The global order of accuracy of the present SBP operator Q is fourth order (Müller, 2008). The energy method and the summation-by-parts operators are discussed in the Appendix A and B, respectively.

Second derivatives of viscous parts of $\hat{\mathbf{F}}_\xi{}'$ and $\hat{\mathbf{G}}_\eta{}'$ are approximated by applying the SBP operator for first derivatives twice. However, successively applying the first derivative operator makes the scheme wider, which requires special treatment for the immersed boundary method, and will be discussed in section boundary conditions below. Spurious high wave number oscillations are suppressed by a sixth order explicit filter (Visbal and Gaitonde, 2002; Müller, 2008). The classical fourth order explicit Runge–Kutta method is employed for time integration.

Immersed boundary formulation

The sharp interface method is well suited for compressible viscous flow, due to imposing the boundary conditions at immersed boundaries, without computing any forcing term and introducing any force distribution function. The ghost point immersed boundary method employed in this study is based on the ghost cell immersed boundary approach for second order methods (Ghias *et al.*, 2007; Mittal *et al.*, 2008).

The basic idea in this method is to compute the value of the flow variables at each of the ghost points (referring to the layer of points inside the solid body adjoining the immersed boundary) such that the boundary conditions at the immersed boundary are satisfied. As illustrated in Fig. 1, the procedure begins by determining the immersed boundary and then distinguishing the solid points, i.e. the nodes lying inside the solid body, and the fluid points, i.e. the nodes lying outside the body in the fluid domain. The ghost points (denoted by GP) are identified by those nodes that lie inside the body and adjacent to the immersed boundary which have at least one neighbour node in the fluid domain with the difference stencil centered at the ghost point. The image point (denoted by IP) can be found by extending a normal probe, i.e. a line normal to the immersed boundary, from the ghost point to intersect with the immersed boundary at the body intercept point (denoted by BI) such that the body intercept point lies at the midpoint of the line connecting the ghost point and the image point. Once the flow variables at the image point are computed, the ghost point variables can be determined by imposing the boundary conditions. In other words, the general strategy is to compute the flow variables at the image point by taking into account the nodal values at the surrounding fluid points and then use the boundary conditions to obtain the values at the ghost point.

Among the available options for determining the flow variables at the image points, the computationally most efficient scheme will be the bilinear interpolation scheme in 2D (Ghias *et al.*, 2007; Mittal *et al.*, 2008) where the flow variables are linearly interpolated from four nodal points surrounding the image points. This interpolation scheme leads to a nominally second order accuracy of the immersed boundary condition. The high order SBP operator used in this study for spatial discretization, corresponding to the sixth order central finite difference method at interior grids, requires three layers of ghost points inside the immersed boundary in order to maintain the overall high order of accuracy, as shown in Fig. 2.

In the case of bilinear interpolation, the interpolating polynomial involves four nodes and hence four nodal values need to be specified. The bilinear interpolation for a generic variable ϕ can be expressed as

$$\phi(x,y) = C_1 + C_2 x + C_3 y + C_4 xy. \tag{5}$$

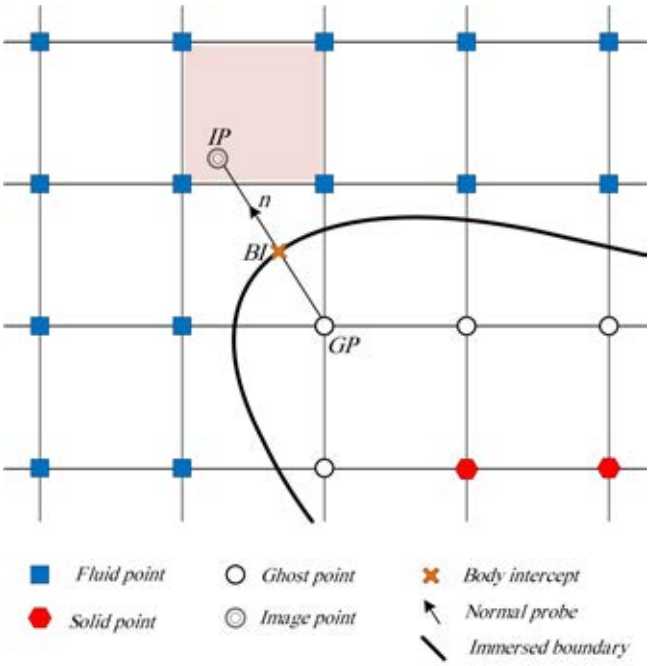

Figure 1: Schematic of points used to interpolate the variable located at a ghost point.

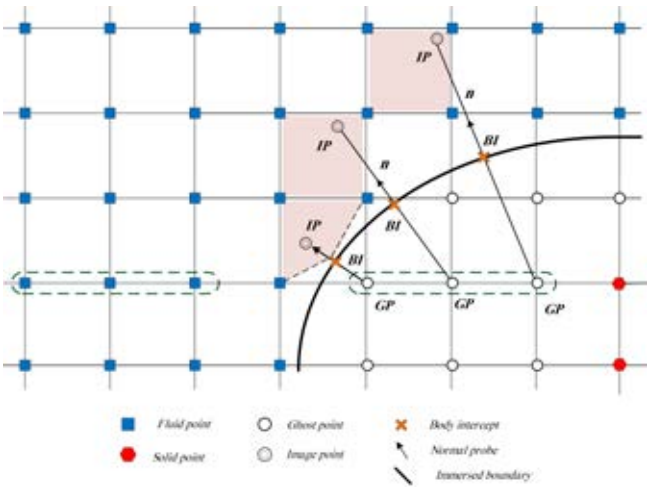

Figure 2: Schematic of 3 layers of ghost points inside immersed body on a Cartesian mesh.

The four unknown coefficients $C_i, i = 1,..,4$, can be determined using values at the four nodes surrounding the image point. Thus, the variable at the image point is reconstructed through bilinear interpolation using unknown coefficients and known flow variables at surrounding fluid nodes. The four weighting coefficients are evaluated as the solution of the linear system

$$\mathbf{VC} = \phi, \tag{6}$$

where

$$\mathbf{C} = \{C_1, C_2, C_3, C_4\}^T \tag{7}$$

is the vector of the unknown coefficients and

$$\phi = \{\phi_1, \phi_2, \phi_3, \phi_4\}^T \tag{8}$$

is the vector of the four surrounding node values. The matrix $\mathbf{V}$ is the Vandermonde matrix which is expressed as

$$\mathbf{V} = \begin{bmatrix} 1 & x_1 & y_1 & x_1 y_1 \\ 1 & x_2 & y_2 & x_2 y_2 \\ 1 & x_3 & y_3 & x_3 y_3 \\ 1 & x_4 & y_4 & x_4 y_4 \end{bmatrix} \tag{9}$$

In this classical formulation, the unknown coefficient values $C_i, i = 1,...,4$, would depend on the solution at each time step. However, the approach can be reformulated such that new coefficients are only dependent on the coordinates of the image point and the geometry of the grids. The reformulation is discussed in detail in Appendix C. Thus, the image point value can be expressed as

$$\phi_{IP} = \sum_{i=1}^{4} \alpha_i \phi_i \tag{10}$$

where $\alpha_i, i = 1,...,4$, are coefficients depending on the coordinates only. They can be established once the grid, immersed boundary and image point coordinates are specified.
When a ghost point is close to the immersed boundary, its corresponding image point might not have four surrounding fluid points. One case would be that the ghost point itself is part of the interpolation scheme. Since the ghost point value in an interpolation scheme would be unknown, the ghost point is then replaced by the body intercept point where the values are determined by the boundary conditions, cf. Fig. 3.
For Dirichlet boundary condition in this case, the corresponding row in Eq. (9) is replaced by

$$\phi_{BI}(x,y) = C_1 + C_2\, x_{BI} + C_3\, y_{BI} + C_4\, x_{BI} y_{BI} \tag{11}$$

where x_{BI} and y_{BI} are the coordinates of the body intercept point. Thereby, for a Dirichlet boundary condition the linear system corresponding to Eq.(6) for this case becomes

$$\begin{bmatrix} 1 & x_1 & y_1 & x_1 y_1 \\ 1 & x_2 & y_2 & x_2 y_2 \\ 1 & x_3 & y_3 & x_3 y_3 \\ 1 & x_B & y_B & x_B y_B \end{bmatrix} \begin{bmatrix} C_1 \\ C_2 \\ C_3 \\ C_4 \end{bmatrix} = \begin{bmatrix} \phi_1 \\ \phi_2 \\ \phi_3 \\ \phi_{BI} \end{bmatrix} \tag{12}$$

For a Neumann boundary condition, the variable gradient at the body intercept is known instead of the actual value. The most obvious choice in such a case is to use the specified gradient value $\frac{\partial \phi_{\mathrm{BI}}}{\partial n}$ to compute the value at the image point. The gradient of ϕ_{BI} at the boundary can be determined by taking the normal derivative of Eq.(11),

$$\frac{\partial \phi_{\mathrm{BI}}}{\partial n} = C_2 n_x + C_3 n_y + C_4 (y_{\mathrm{BI}} n_x + x_{\mathrm{BI}} n_y) = \zeta \tag{13}$$

where n_x and n_y are the components of the unit vector normal to the boundary.
Thus, the linear system corresponding to Eq.(6) for this case becomes

$$\begin{bmatrix} 1 & x_1 & y_1 & x_1 y_1 \\ 1 & x_2 & y_2 & x_2 y_2 \\ 1 & x_3 & y_3 & x_3 y_3 \\ 0 & n_x & n_y & y_{BI} n_x + x_{BI} n_y \end{bmatrix} \begin{bmatrix} C_1 \\ C_2 \\ C_3 \\ C_4 \end{bmatrix} = \begin{bmatrix} \phi_1 \\ \phi_2 \\ \phi_3 \\ \zeta \end{bmatrix} \tag{14}$$

As shown in Fig. 4, it might also be the case that two interpolation points would lie inside the immersed body, one at the corresponding ghost point itself and one at another ghost point. The procedure we used to handle this case is to repeat the above steps for the other ghost point as well, resulting in a Vandermonde matrix where another row is also replaced by Eqs. (11) or (13) in the same way as the fourth row, in contrast to (Ghias *et al.*, 2007; Mittal *et al.*, 2008). Applying our procedure for this case, it is no longer necessary to solve a coupled linear system by using iterative processes like (Ghias *et al.*, 2007; Mittal *et al.*, 2008). This situation does not pose any consistency issues and ensures that the interpolation procedure for the image point is well-posed without affecting the accuracy of the interpolation.
The value of the variable at the ghost point is computed by employing a linear approximation along the normal probe which takes into account the boundary condition at the boundary intercept. For a Dirichlet boundary condition this can generally be expressed as

$$\phi_{\mathrm{BI}} = \tfrac{1}{2}(\phi_{\mathrm{IP}} + \phi_{\mathrm{GP}}) + O(\triangle l^2) \tag{15}$$

where $\triangle l$ is the length of the normal probe from GP to IP. Solving for ϕ_{GP} using Eq. (15) and neglecting the truncation gives

$$\phi_{\mathrm{GP}} = \left(2 - \sum_{j \in \mathcal{G}} \alpha_j\right) \phi_{\mathrm{BI}} - \sum_{i \notin \mathcal{G}} \alpha_i \phi_i \tag{16}$$

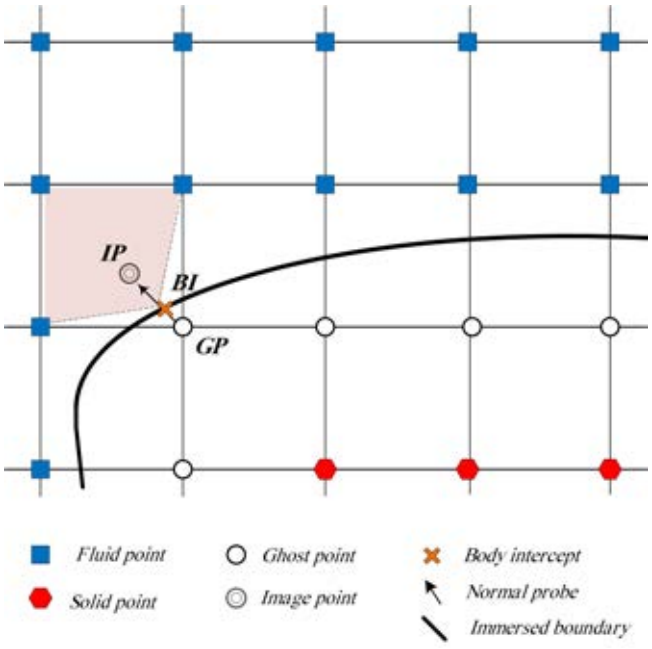

Figure 3: Schematic of the situation when one surrounding interpolation point is the boundary intercept.

where $\mathcal{G}$ is the set of body intercepts that are part of the interpolation stencil. For a Neumann boundary condition on the immersed boundary, the following second-order central-difference is written along the normal probe

$$(\frac{\partial \phi}{\partial n})_{\mathrm{BI}} = \frac{\phi_{\mathrm{IP}} - \phi_{\mathrm{GP}}}{\triangle l} + O(\triangle l^2) \tag{17}$$

Thereby, the general formulation for a non-homogeneous Neumann boundary condition is expressed as

$$\phi_{\mathrm{GP}} = \left(\sum_{j \in \mathcal{G}} \alpha_j - \triangle l \right) (\frac{\partial \phi}{\partial n})_{\mathrm{BI}} + \sum_{i \notin \mathcal{G}} \alpha_i \phi_i \tag{18}$$

Boundary conditions

The no-slip boundary condition at the immersed boundary for a stationary body is considered. Thereby, Dirichlet boundary conditions are employed for the velocity components at the IB. For each velocity components, the corresponding value at the body intercept $\phi_{BI} = 0$ is set in Eq. (11). Applying the no-slip condition at the body surface, the convective flux contribution should be zero. The pressure gradient normal to the immersed interface is set zero as a boundary layer approximation, $\frac{\partial p}{\partial n} = \frac{\partial \phi_{\mathrm{BI}}}{\partial n} = 0$ in Eq. (13). The boundary condition for the temperature depends on the whether the immersed surface of the body is adiabatic or isothermal. Assuming an adiabatic boundary condition at the immersed body, the temperature gradient normal to the surface $\frac{\partial T}{\partial n} = 0$ is set to zero by enforcing a zero density gradient $\frac{\partial \rho}{\partial n} = 0$. Thus, for the variables ρ and p Neumann boundary conditions are employed. According to the boundary conditions considered for the immersed body, the values of the conservative perturbation variables at the ghost points are determined once the flow variables at the image points

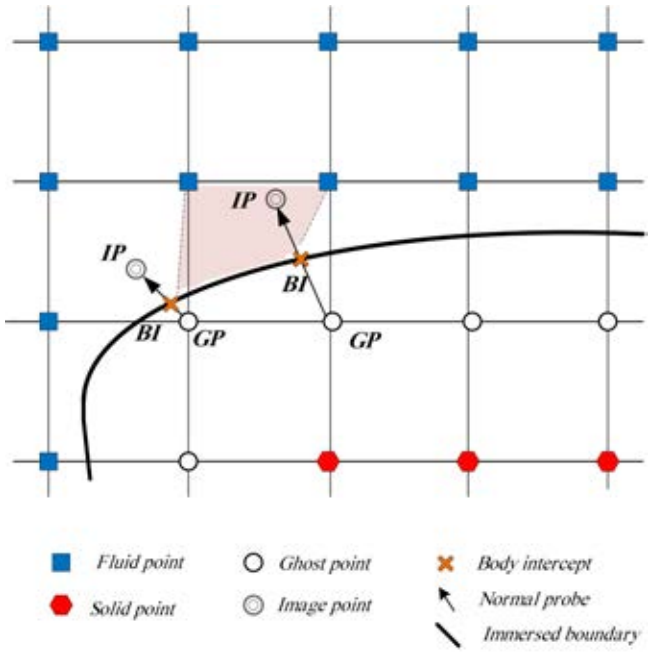

Figure 4: Schematic of the situation when two of the surrounding interpolation points lie inside the immersed body.

are interpolated using:

$$\begin{aligned} \rho'_{GP} &= \rho'_{IP} \\ (\rho u)'_{GP} &= -(\rho u)'_{IP} \\ (\rho v)'_{GP} &= -(\rho v)'_{IP} \\ (\rho E)'_{GP} &= (\rho E)'_{IP} \end{aligned} \tag{19}$$

As mentioned above, applying the first derivative approximation twice for computing the second derivative will make the stencil wider. For the proper treatment of wide stencils in computing the second derivative, the first derivatives of the viscous terms are computed up to and including the ghost points, treating the solid points inside the ghost point layers as domain boundaries when employing the differencing stencil. Using this procedure, we ensure that the derivatives of the viscous fluxes at the fluid points closest to the immersed boundary are computed with high order.

Non-reflecting characteristic boundary conditions are employed at the inflow and outflow boundaries to minimize wave reflections. The Navier–Stokes characteristic boundary conditions (NSCBC) developed by (Poinsot and Lele, 1992) are employed to approximate incoming waves based on local one-dimensional inviscid (LODI) relations. The primitive variables can be related to the wave amplitude ($\mathscr{L}_i$) by LODI relations. The amplitudes of the characteristic waves are $\mathscr{L}_1 = \lambda_1(\frac{\partial p}{\partial x} - \rho c \frac{\partial u}{\partial x})$, $\mathscr{L}_2 = \lambda_2(c^2 \frac{\partial \rho}{\partial x} - \frac{\partial p}{\partial x})$, $\mathscr{L}_3 = \lambda_3(\frac{\partial v}{\partial x})$ and $\mathscr{L}_4 = \lambda_4(\frac{\partial p}{\partial x} + \rho c \frac{\partial u}{\partial x})$. Since fully non-reflecting conditions may lead to an ill-posed problem (Poinsot and Lele, 1992), this approach is partially reflecting. Imposing a constant pressure at the outlet requires $\mathscr{L}_1 = -\mathscr{L}_4$. To keep the reflections low and the pressure close to atmospheric pressure, the incoming wave amplitude is set to

$$\mathscr{L}_1 = K(p - p_{\mathrm{atm}}) \tag{20}$$

where K is a relaxation coefficient. Rudy and Strikwerda proposed the relaxation coefficient as $K = \Lambda(1 - \mathrm{Ma}^2)(c/L_t)$ where Ma is the Mach number, c the speed of sound, L_t the total length of the domain and Λ a parameter (Rudy and Strikwerda, 1980). The optimum value $\Lambda = 0.25$ derived by (Rudy and Strikwerda, 1980) is employed. For reverse flow (negative velocity in x-direction) at the outlet, $\mathscr{L}_1$, $\mathscr{L}_2$ and $\mathscr{L}_3$ are set to zero. A similar boundary treatment at inflow and outflow was used by (Khalili *et al.*, 2016).

RESULTS

In order to assess the accuracy of the immersed boundary methodology, a two-dimensional steady state heat problem is first solved. Then, the IBM is applied to a two-dimensional flow past a circular cylinder at a range Reynolds numbers to demonstrate the ability and performance of the method for simulating compressible viscous flow.

Steady state heat equation

To verify the order of spatial accuracy of the current immersed boundary scheme, a steady state heat transfer problem has been considered. Since the ghost point immersed boundary method is second-order accurate (Ghias *et al.*, 2007; Mittal *et al.*, 2008), care has been taken to maintain a second-order spatial accuracy in the imposition of boundary conditions on the immersed boundary. The steady state heat equation reads

$$\nabla^2 T = \sigma \tag{21}$$

where σ is a source term, i.e. $-\kappa\sigma$ is the rate of heat generation per unit volume. The exact solution for this case in polar coordinates can be expressed as

$$T(r) = \sigma \frac{r^2}{4} + A \ln(r) + B \tag{22}$$

where A and B depend on the boundary conditions type and their values.

The numerical solution by means of IBM is implemented to solve Eq.(21) in Cartesian coordinates. The second and fourth order central finite difference methods for second derivatives are employed for spatial discretization of the regular fluid points.

$$T_{xx}^{(2)} = (T_{i+1} - 2T_i + T_{i-1})/\Delta x^2 \tag{23}$$

$$T_{xx}^{(4)} = (-T_{i+2} + 16T_{i+1} - 30T_i + 16T_{i-1} - T_{i-2})/(12\Delta x^2) \tag{24}$$

The temperature distribution is solved between two concentrical cylinders with inner and outer diameters $D_{\text{inner}} = 3.5$ and $D_{\text{outer}} = 8.5$, respectively, embedded in a square domain of edge length $L = 10$. The $\sigma = -0.45$ is chosen and the temperatures of the inner and outer cylinders are $T_{\text{inner}} = 5$ and $T_{\text{outer}} = 10$, respectively. The immersed boundary approach is implemented at the cylinder interfaces. The results from different grids on a uniform Cartesian grid ($N \times N$) from $N = 100$ to 1000 are compared with the exact solution to compute the L_2 and L_∞ norms. Fig. 5 shows the errors for different grids.

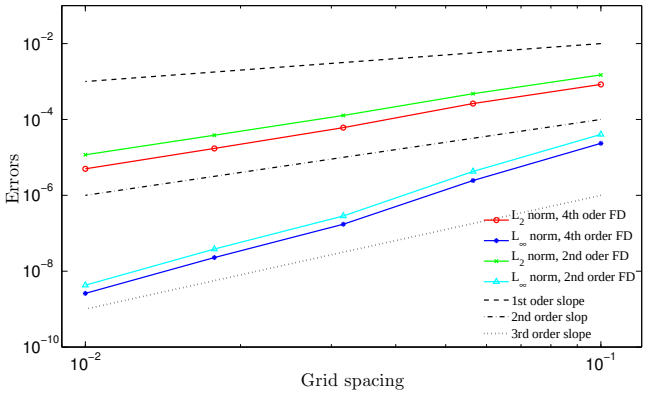

Figure 5: L_2 and L_∞ norms computed at various grid levels with IBM for 2D steady heat Eq. (21).

The first, second and third–order convergence rates are also included in Fig. 5 for reference. This figure indicates that a second-order rate of convergence has been achieved by the Poisson solver for Dirichlet boundary conditions at immersed boundaries. The error are slightly lower for the fourth order difference method than for the second order one.

Flow past circular cylinder

To verify and validate the present immersed boundary treatment for a compressible flow solver, the benchmark flow over a circular cylinder is firstly simulated at the Reynolds numbers of 20 and 40 based on the free-stream velocity and diameter of the cylinder. It is known that steady flow over a circular cylinder can persist up to Reynolds numbers of about 40. The free-stream Mach number for the simulation is set as a small number Ma = 0.03 in order to be comparable to the simulations performed using incompressible solvers. Then, the unsteady flow over a circular cylinder has been chosen to verify the proposed IB method at the Reynolds number of 100 and Mach number 0.25.

The computational domain size is $90D \times 40D$ where D is the diameter of the cylinder. The center of the cylinder is located at the point $(20D, 20D)$ of the coordinate system. The computational domain is sizeable to reduce the effects of domain boundaries and wave reflections form the inlet and outlet boundaries. It has been observed that those could lead to a momentous error when computing the lift and drag coefficients. In the present work, the block structured computational domain has been discretized with non-uniform Cartesian grids, where the block corresponding to the cylinder has a much finer grid spacing of ($\Delta x = \Delta y = D/25$) at Re = 20 and 40, and grid spacing of ($\Delta x = \Delta y = D/50$) at Re = 100. At these grid resolutions, the lift and drag coefficients are sufficiently converged. Sufficient grid resolution around the cylinder is crucial to obtain the drag and lift coefficients accurately. Additionally, to capture the von Kármán vortex shedding, the wake region needs to be resolved properly. The grid spacing Δx and Δy was smoothly stretched from ($\Delta x = \Delta y = D/25$ at Re = 20 and 40, and $\Delta x = \Delta y = D/50$ for Re=100 to $\Delta x = \Delta y = D/2$ near the inflow, outflow, top and bottom boundaries. Symmetry boundary conditions are applied on the top and bottom of the computational domain. At the inflow, the velocities in the x- and y-directions are imposed using a uniform inlet profile normal to the boundary, $u(x = 0, t) = U_\infty$ and $v = 0$. In addition, the inlet temperature is set to $T = T_0 = 310$ K. The outlet pressure is set to atmospheric pressure, i.e., $p' = p - p_0 = p - p_{\text{atm}} = 0$ Pa.

The drag and lift coefficients are defined as $C_D = \frac{F_D}{\frac{1}{2}\rho_\infty U_\infty^2 D}$ and $C_L = \frac{F_L}{\frac{1}{2}\rho_\infty U_\infty^2 D}$, respectively, where F_D and F_L are the drag and lift forces. The total force on the cylinder is given by the sum of the pressure and viscous force integrated over the cylinder surface $F = -\oint p_B \cdot \mathbf{n}\, ds + \oint \tau_B \cdot \mathbf{n}\, ds$ where $\mathbf{n}$ is the outer unit vector normal to the cylinder, and p_B and τ_B are pressure and the viscous stress tensor on the body surface, respectively. These quantities are based on the evaluation of surface pressure and viscous stress. The procedure used to compute these surface quantities needs some explanation. In the current solver, four nodes surrounding a body-intercept point corresponding to the first layer of ghost points are identified and then a bilinear interpolation is used to estimate the pressure and viscous stress tensor at the body intercept. The viscous stress at the involved ghost points and fluid points are computed in a straightforward manner by using our high order method.

Figs. 6 - 9 show streamlines and vorticity contours for Re = 20 and Re = 40, respectively. The geometrical properties of the vortices behind the cylinder are schematically illustrated in Fig. 10 (Canuto and Taira, 2015). The quantitative comparison of these parameters as well as the drag coefficient with available numerical and experimental results are given in Table 1.

Fig. 11 presents the instantaneous spanwise vorticity ω_z contours for Re = 100 indicating the presence of the von Kármán vortex street. The vortex shedding leads to time-varying lift and drag forces until they reach to a periodic oscillatory form. The Strouhal number $St = \frac{fD}{U_\infty}$, where f is the vortex sheding frequency, is computed from the temporal variation of the lift coefficient. Due to the unsteadiness of the flow, the comparison of the average values of the lift and drag coefficients as well as the amplitude of the sinusoidal variation in time of the lift and drag coefficients is central. The results for the time-averaged lift and drag coefficients, the amplitude of

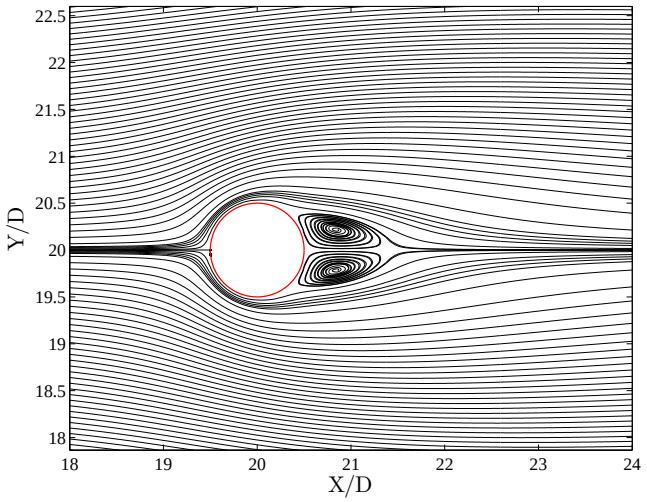

Figure 6: Streamlines for computed flow past a circular cylinder at Re = 20 and Ma = 0.03.

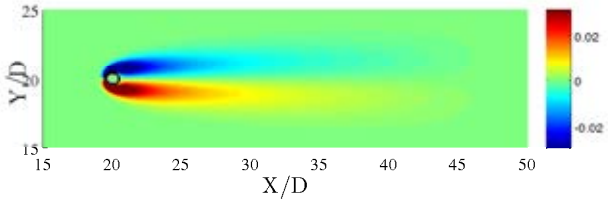

Figure 7: Vorticity contours for computed flow past a circular cylinder at Re = 20 and Ma = 0.03.

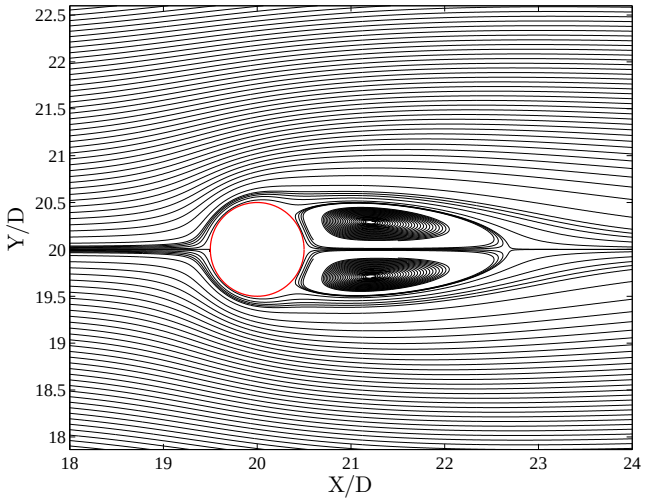

Figure 8: Streamlines for computed flow past a circular cylinder at Re = 40 and Ma = 0.03.

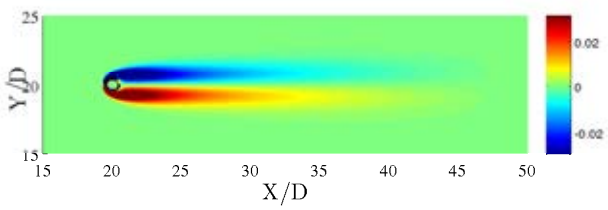

Figure 9: Vorticity contours for computed flow past a circular cylinder at Re = 40 and Ma = 0.03.

Table 1: Comparison of computed data with available numerical and experimental data at Re = 20 and Re = 40. (Exp.) indicates the experimental results.

	Re = 20					
	Ma	L	a	b	$\theta(deg)$	C_D
(Tritton, 1959)(Exp.)	-	-	-	-	-	2.09
(Dennis and Chang, 1970)	0	0.94	-	-	43.7	2.05
(Coutanceau and Bouard, 1977)(Exp.)	-	0.93	0.33	0.46	45.0	-
(Fornberg, 1980)	0	0.91	-	-	45.7	2.0
(Linnick and Fasel, 2003)	0	0.93	0.36	0.43	43.5	2.06
(De Palma *et al.*, 2006)	0.03	0.93	0.36	0.43	44.6	2.05
(Canuto and Taira, 2015)	0	0.92	0.36	0.42	43.7	2.07
Present study	**0.03**	**0.93**	**0.36**	**0.43**	**43.9**	**2.05**
	Re = 40					
	Ma	L	a	b	$\theta(deg)$	C_D
(Tritton, 1959)(Exp.)	-	-	-	-	-	1.59
(Dennis and Chang, 1970)	0	2.35	-	-	53.8	1.52
(Coutanceau and Bouard, 1977)(Exp.)	-	2.13	0.76	0.59	53.8	-
(Fornberg, 1980)	0	2.24	-	-	55.6	1.50
(Linnick and Fasel, 2003)	0	2.28	0.72	0.60	53.6	1.52
(De Palma *et al.*, 2006)	0.03	2.28	0.72	0.60	53.8	1.55
(Canuto and Taira, 2015)	0	2.24	0.72	0.59	53.7	1.54
Present study	**0.03**	**2.22**	**0.72**	**0.59**	**53.1**	**1.52**

their changes as well as the Strouhal number of the present study are compared to published results in Table 2. Table 1 and 2 confirm that for the present study all results compare very well with results reported in the literature.

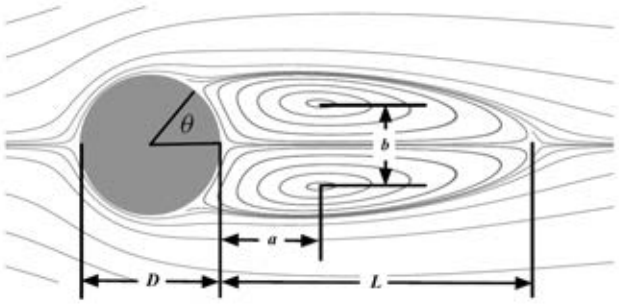

Figure 10: Definitions of the relevant geometrical parameters of the symmetric deperation region behind the cylinder (Canuto and Taira, 2015).

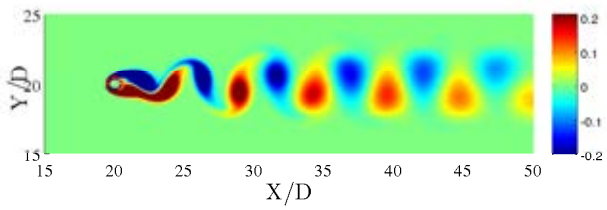

Figure 11: Vorticity contours for computed flow past a circular cylinder at Re = 100 and Ma = 0.25

Table 2: Comparison of computed data with available numerical and experimental data at Re = 100.

Re = 100				
	Ma	*St*	C_D	C_L
(Berger and Wille, 1972)	0	0.16-0.17	-	-
(Liu *et al.*, 1998)	0	0.165	1.35 ± 0.012	± 0.339
(Linnick and Fasel, 2003)	0	0.166	1.34 ± 0.009	± 0.333
(Mittal *et al.*, 2008)	0	-	1.35	-
(Karagiozis *et al.*, 2010)	0.25	0.168	1.336	± 0.319
(Canuto and Taira, 2015)	0.25	0.163	1.378	± 0.325
Present study	**0.25**	**0.1667**	$\mathbf{1.33 \pm 0.013}$	$\mathbf{\pm 0.323}$

CONCLUSION

In this paper, we have combined highly stable high-order SBP operators with an immersed boundary method which permits us to use Cartesian grids for arbitrary geometries for solving the compressible Navier–Stokes equations accurately and efficiently. SBP operators which are 6^{th} order accurate in the interior and 3^{rd} order accurate near the boundaries is employed. To achieve high accuracy and easy parallelization, the 4^{th} order explicit Runge–Kutta method is applied. The methodology is applied to compute steady and unsteady flow problems to demonstrate its versatility as well as its accuracy. The flow past a circular cylinder for moderate values of Reynolds number and Mach number is assessed. A good agreement with available experimental and numerical results is achieved.

ACKNOWLEDGMENTS

The present research is a part of a research project entitled "Modeling of obstructive sleep apnea by fluid-structure interaction in the upper airways" funded by the Research Council of Norway. The simulations in our work are done on the Vilje cluster at NTNU which is gratefully acknowledged.

REFERENCES

BALARAS, E. (2004). "Modeling complex boundaries using an external force field on fixed Cartesian grids in large-eddy simulations". *Computers & Fluids*, **33(3)**, 375–404.

BERGER, E. and WILLE, R. (1972). "Periodic flow phenomena". *Annual Review of Fluid Mechanics*, **4(1)**, 313–340.

BREHM, C., HADER, C. and FASEL, H.F. (2015). "A locally stabilized immersed boundary method for the compressible navier–stokes equations". *Journal of Computational Physics*, **295**, 475–504.

CANUTO, D. and TAIRA, K. (2015). "Two-dimensional compressible viscous flow around a circular cylinder". *Journal of Fluid Mechanics*, **785**, 349–371.

COUTANCEAU, M. and BOUARD, R. (1977). "Experimental determination of the main features of the viscous flow in the wake of a circular cylinder in uniform translation. Part 1. Steady flow". *Journal of Fluid Mechanics*, **79(02)**, 231–256.

DE PALMA, P., DE TULLIO, M., PASCAZIO, G. and NAPOLITANO, M. (2006). "An immersed-boundary method for compressible viscous flows". *Computers & Fluids*, **35(7)**, 693–702.

DE TULLIO, M.D., DE PALMA, P., IACCARINO, G., PASCAZIO, G. and NAPOLITANO, M. (2007). "An immersed boundary method for compressible flows using local grid refinement". *Journal of Computational Physics*, **225(2)**, 2098–2117.

DENNIS, S. and CHANG, G.Z. (1970). "Numerical solutions for steady flow past a circular cylinder at Reynolds numbers up to 100". *Journal of Fluid Mechanics*, **42(03)**, 471–489.

FADLUN, E., VERZICCO, R., ORLANDI, P. and MOHD-YUSOF, J. (2000). "Combined immersed-boundary finite-difference methods for three-dimensional complex flow simulations". *Journal of Computational Physics*, **161(1)**, 35–60.

FORNBERG, B. (1980). "A numerical study of steady viscous flow past a circular cylinder". *Journal of Fluid Mechanics*, **98(04)**, 819–855.

GHIAS, R., MITTAL, R. and DONG, H. (2007). "A sharp interface immersed boundary method for compressible viscous flows". *Journal of Computational Physics*, **225(1)**, 528–553.

GOLDSTEIN, D., HANDLER, R. and SIROVICH, L. (1993). "Modeling a no-slip flow boundary with an external force field". *Journal of Computational Physics*, **105(2)**, 354–366.

GUSTAFSSON, B. (2008). *High order difference methods for time dependent PDE*. Springer, Berlin.

GUSTAFSSON, B., KREISS, H.O. and OLIGER, J. (1995). *Time dependent problems and difference methods*. John Wiley & Sons, New York.

HAERI, S. and SHRIMPTON, J. (2012). "On the application of immersed boundary, fictitious domain and body-conformal mesh methods to many particle multiphase flows". *International Journal of Multiphase Flow*, **40**, 38 – 55.

KARAGIOZIS, K., KAMAKOTI, R. and PANTANO, C. (2010). "A low numerical dissipation immersed interface method for the compressible navier–stokes equations". *Journal of Computational physics*, **229(3)**, 701–727.

KHALILI, M., LARSSON, M. and MÜLLER, B. (2016). "Interaction between a simplified soft palate and compressible viscous flow". *Journal of Fluids and Structures*, **67**, 85–105.

LARSSON, M. and MÜLLER, B. (2009). "Numerical simulation of confined pulsating jets in human phonation". *Computers & Fluids*, **38(7)**, 1375–1383.

LINNICK, M. and FASEL, H. (2003). "A high-order immersed boundary method for unsteady incompressible flow calculations". *41st Aerospace Sciences Meeting and Exhibit*, 1124.

LIU, C., ZHENG, X. and SUNG, C. (1998). "Preconditioned multigrid methods for unsteady incompressible flows". *Journal of Computational Physics*, **139(1)**, 35–57.

MITTAL, R. and IACCARINO, G. (2005). "Immersed boundary methods". *Annual Review of Fluid Mechanics*, **37**, 239–261.

MITTAL, R., DONG, H., BOZKURTTAS, M., NAJJAR, F., VARGAS, A. and VON LOEBBECKE, A. (2008). "A versatile sharp interface immersed boundary method for incompressible flows with complex boundaries". *Journal of Computational Physics*, **227(10)**, 4825–4852.

MOHD-YUSOF, J. (1997). "Combined immersed-boundary/B-spline methods for simulations of flow in complex geometries". *Center for Turbulence Research Annual Research Briefs*, 317–325.

MÜLLER, B. (2008). "High order numerical simulation of aeolian tones". *Computers & Fluids*, **37(4)**, 450–462.

PESKIN, C.S. (1972). "Flow patterns around heart valves: A numerical method". *Journal of Computational Physics*, **10(2)**, 252–271.

POINSOT, T.J. and LELE, S. (1992). "Boundary conditions for direct simulations of compressible viscous flows". *Journal of Computational Physics*, **101(1)**, 104–129.

RUDY, D.H. and STRIKWERDA, J.C. (1980). "A non-reflecting outflow boundary condition for subsonic Navier-Stokes calculations". *Journal of Computational Physics*, **36(1)**, 55–70.

SAIKI, E. and BIRINGEN, S. (1996). "Numerical simulation of a cylinder in uniform flow: Application of a virtual boundary method". *Journal of Computational Physics*, **123(2)**, 450–465.

SESTERHENN, J., MÜLLER, B. and THOMANN, H. (1999). "On the cancellation problem in calculating compressible low Mach number flows". *Journal of Computational Physics*, **151(2)**, 597–615.

SOTIROPOULOS, F. and YANG, X. (2014). "Immersed boundary methods for simulating fluid-structure interaction". *Progress in Aerospace Sciences*, **65**, 1 – 21.

STRAND, B. (1994). "Summation by parts for finite difference approximations for d/dx". *Journal of Computational Physics*, **110(1)**, 47–67.

SVÄRD, M. and NORDSTRÖM, J. (2014). "Review of summation-by-parts schemes for initial–boundary-value problems". *Journal of Computational Physics*, **268**, 17–38.

TRITTON, D. (1959). "Experiments on the flow past a circular cylinder at low Reynolds numbers". *Journal of Fluid Mechanics*, **6(04)**, 547–567.

TSENG, Y.H. and FERZIGER, J.H. (2003). "A ghost-cell immersed boundary method for flow in complex geometry". *Journal of Computational Physics*, **192(2)**, 593–623.

VISBAL, M.R. and GAITONDE, D.V. (2002). "On the use of higher-order finite-difference schemes on curvilinear and deforming meshes". *Journal of Computational Physics*, **181(1)**, 155–185.

YE, T., MITTAL, R., UDAYKUMAR, H. and SHYY, W. (1999). "An accurate Cartesian grid method for viscous incompressible flows with complex immersed boundaries". *Journal of Computational Physics*, **156(2)**, 209–240.

APPENDIX A. ENERGY METHOD

To demonstrate the energy method, we apply the procedure to a simplified PDE, that is, rather than analysing the full Navier–Stokes equations in this section, we only focus on the 1D convection–diffusion equation as a model equation.

$$\begin{aligned} &u_t + au_x = bu_{xx}, \quad 0 \le x \le 1 \quad t \ge 0 \\ &u(x,0) = f(x) \\ &u(0,t) = u(1,t) = g(t) = 0 \end{aligned} \tag{25}$$

where a and b are assumed to be constant and positive, and u is the dependent variable. The L_2 scalar product for two real functions v and w is defined by

$$(v,w) = \int_0^1 v(x)w(x)dx \tag{26}$$

which then defines the L_2 norm of the continuous solution at time t and energy $E(t) = \|u(\cdot,t)\|^2 = (u,u)$. Using integration by parts $(v,w_x) = v(1,t)w(1,t) - v(0,t)w(0,t) - (v_x,w)$, the energy method leads to

$$\begin{aligned} &\tfrac{dE}{dt} = \tfrac{d}{dt}\|u(\cdot,t)\|^2 = (u_t,u) + (u,u_t) \\ &= (-au_x + bu_{xx}, u) + (u, -au_x + bu_{xx}) \\ &= -a[u^2(1,t) - u^2(0,t)] + 2b[u(1,t)u_x(1,t) - u(0,t)u_x(0,t)] \\ &-2b(u_x,u_x) \le au^2(0,t) + 2b[u(1,t)u_x(1,t) - u(0,t)u_x(0,t)] \\ &= 0 \end{aligned} \tag{27}$$

which yields a non growing solution, i.e. $E(t) \le E(0) = \|f(x)\|^2$. Thus, the energy is bounded by the initial condition.

APPENDIX B. SUMMATION BY PARTS OPERATORS

(Khalili *et al.*, 2016)

The SBP operators are constructed to guarantee a discrete energy estimate similar to the continuous energy estimate above.

$$\begin{aligned} &u_t + au_x = bu_{xx}, \quad 0 \le x \le 1 \quad t \ge 0 \\ &u(x,0) = f(x) \\ &u(0,t) = u(1,t) = g(t) = 0 \end{aligned} \tag{28}$$

where a and b are assumed to be constant and positive, and u is the dependent variable.

The basis of getting such an energy estimate is to satisfy integration by parts in the discrete sense called Summation–By–Parts (SBP) property (Gustafsson, 2008; Svärd and Nordström, 2014). To outline this technique for model problem (28), we consider $u_j = u_j(t)$ the numerical solution of the convection–diffusion equation at grid point $x_j = jh, j = 0,...,N$, with grid spacing $h = \frac{1}{N}$. The solution vector containing the solution at the discrete grid points is $\mathbf{u} = [u_0(t), u_1(t), ..., u_N(t)]^T$. Using a difference operator Q approximating the first derivative in space, the semi-discrete form of the model equation can be expressed as

$$\tfrac{d\mathbf{u}}{dt} = -aQ\mathbf{u} + bQQ\mathbf{u}, \quad u_j(0) = f(x_j) \tag{29}$$

The discrete scalar product and corresponding norm and energy can be defined by

$$\begin{aligned} &(\mathbf{u},\mathbf{v})_h = h\mathbf{u}^T H\mathbf{v}, \\ &E_h(t) = \|\mathbf{u}\|_h^2 = (\mathbf{u},\mathbf{u})_h \end{aligned} \tag{30}$$

where H is a diagonal and positive definite matrix defined by $H = \mathrm{diag}(H_L, I, H_R)$. The SBP property is satisfied by the difference operator Q, if

$$(\mathbf{u}, Q\mathbf{v})_h = u_N v_N - u_0 v_0 - (Q\mathbf{u}, \mathbf{v})_h \tag{31}$$

or if Q can be written on the form $hQ = H^{-1}P$ for P satisfying

$$P + P^T = E_N - E_0 = \mathrm{diag}(-1,0,...,0,1) \tag{32}$$

where $E_0 = \mathrm{diag}(1,0,...,0)$ and $E_N = \mathrm{diag}(0,0,...,1)$. Using the semi–discrete equation 29, the energy estimate for the semi–discrete problem can be obtained as

$$\begin{aligned} &\tfrac{dE}{dt} = \tfrac{d}{dt}\|u(\cdot,t)\|^2 = (u_t,u)_h + (u,u_t)_h \\ &= (-aQu + bQQu, u)_h + (u, -aQu + bQQu)_h \\ &= -a[u_N^2 - u_0^2] + 2b[u_N(Qu)_N - u_0(Qu)_0] \\ &-2b(Qu,Qu)h \le au_0^2 + 2b[u_N(Qu)_N - u_0(Qu)_0]. \end{aligned} \tag{33}$$

We would get non-growing energy in time if the homogeneous boundary conditions could directly be imposed in (33). However, this will change the difference operator Q such that its SBP property might be lost. To avoid this problem, boundary conditions are weakly imposed by the simultaneous approximation term (SAT) technique (Gustafsson, 2008). A first derivative SBP operator with diagonal quadrature matrix H in 30 is a $O(h^{2s})$ accurate central difference operator which is $O(h^s)$ accurate at and near boundaries $s = 1,2,3$. Such an SBP operator is globally $O(h^{s+1})$ accurate.

APPENDIX C. REFORMULATION OF COEFFICIENTS

The four unknown coefficients $C_i, i = 1,..,4$ can be determined using values of the four variables surrounding the image point. It can be expressed as

$$\mathbf{C} = \mathbf{V}^{-1}\{\phi\} \tag{34}$$

where $\mathbf{V}$ is the Vandermonde matrix corresponding to the bilinear interpolation scheme for four surrounding nodes. The value at the image point can be expressed as

$$\phi_{\mathrm{IP}} = \begin{bmatrix} 1 & x_{\mathrm{IP}} & y_{\mathrm{IP}} & x_{\mathrm{IP}}y_{\mathrm{IP}} \end{bmatrix} \begin{bmatrix} C_1 \\ C_2 \\ C_3 \\ C_4 \end{bmatrix} \tag{35}$$

The vector in bracket can be expressed as

$$\mathbf{V}_{\mathrm{IP}} = \begin{bmatrix} 1 & x_{\mathrm{IP}} & y_{\mathrm{IP}} & x_{\mathrm{IP}}y_{\mathrm{IP}} \end{bmatrix} = \sum_{i=1}^{4} \alpha_i V_i \tag{36}$$

where V_i is the ith row of $\mathbf{V}$ and α_i depends on the coordinates of the image point and the four surrounding nodes.
Thereby, the matrix equation for α can be written as

$$\begin{bmatrix} 1 \\ x_{\mathrm{IP}} \\ y_{\mathrm{IP}} \\ x_{\mathrm{IP}}y_{\mathrm{IP}} \end{bmatrix} = \begin{bmatrix} 1 & 1 & 1 & 1 \\ x_1 & x_2 & x_3 & x_4 \\ y_1 & y_2 & y_3 & y_4 \\ x_1y_1 & x_2y_2 & x_3y_3 & x_4y_4 \end{bmatrix} \begin{bmatrix} \alpha_1 \\ \alpha_2 \\ \alpha_3 \\ \alpha_4 \end{bmatrix} \tag{37}$$

By rearranging, α can be obtained as

$$\alpha = \mathbf{V}^{-T}\mathbf{V}_{\mathrm{IP}}^{T}. \tag{38}$$

Thus, the value at the image point can be expressed as

$$\phi_{\mathrm{IP}} = \phi^{T}\mathbf{V}^{-T}\mathbf{V}_{\mathrm{IP}}^{T} \tag{39}$$

Inserting the result obtained in Eq. (38), the value at the image point can obtained be as

$$\phi_{\mathrm{IP}} = \sum_{i=1}^{4} \alpha_i \phi_i \tag{40}$$